

Shuping Hou
Zejiang Zhang
Hongtai Lian
Xiaodong Xing
Haixia Gong
Xiujun Xu



<http://dx.doi.org/10.21278/brod73307>

ISSN 0007-215X
eISSN 1845-5859

HULL SHAPE OPTIMIZATION OF SMALL UNDERWATER VEHICLE BASED ON KRIGING-BASED RESPONSE SURFACE METHOD AND MULTI-OBJECTIVE OPTIMIZATION ALGORITHM

UDC 629.5.015.2:629.5.013.2:005.591.1

Original scientific paper

Summary

Small underwater vehicles have unique advantages in ocean exploration. The resistance and volume of a vehicle are key factors affecting its operation time underwater. This paper aims to develop an effective method to obtain the optimal hull shape of a small underwater vehicle using Kriging-based response surface method (RSM) and multi-objective optimization algorithm. Firstly, the hydrodynamic performance of a small underwater vehicle is numerically investigated using computational fluid dynamics (CFD) method and the value range of related design variables is determined. The mesh convergence is verified to ensure the accuracy of the calculation results. Then, by means of the Latin hypercube sampling (LHS) design of simulation, the Kriging-based RSM model is developed according to the relation between each design variable of the vehicle and the output parameters applied to the vehicle. Based on the Kriging-based RSM model, the optimal hull shape of the vehicle is determined by using Screening and MOGA. As results, the vehicle resistance reduces and volume increases obviously.

Keywords: resistance; volume; small underwater vehicle; Kriging-based response surface method; CFD; multi-objective optimization algorithm

1. Introduction

The ocean is an important asset for the sustainable development of human society [1], and investment in marine surveying and naval equipment manufacturing is increasing in various countries. Underwater vehicles are suitable for surveying, photographing, and collecting information in deep water areas. Therefore, their application fields are gradually expanding, including underwater observation, underwater reconnaissance, aquaculture, underwater military and so on. Small underwater vehicles have unique advantages in both civilian and military applications due to their outstanding concealment [2, 3].

Due to the small size of underwater vehicles, they cannot carry excess energy supply [4]. As a result, it is necessary for small underwater vehicles to overcome as little resistance as possible when moving underwater. Optimizing the hull shape of small underwater vehicles can effectively reduce their resistance from water. As an important tool for underwater vehicles analysis [5-8], computational fluid dynamics (CFD) has been introduced into the underwater vehicle resistance analysis process because of its efficient, accurate and fast calculations. Rans equations and three different turbulence including RKE, SSTKO and RSM were used for the description of turbulent flow in [9]. The authors studied the influence of bow on three ship types. The results showed that the experimental and numerical results are similar and the total resistance decreased 7% using bulbous bow. Ignacio et al. [10] used Navier-Stokes equations with Favre's average and $k-\varepsilon$ model in SolidWorks Flow Simulation. The design variables of an autonomous underwater vehicle (AUV) of torpedo body type was optimized and the expected low resistance was verified through the experiment. The authors of [11] used RANS equations and SST $k-\omega$ model. And a parallel multidisciplinary optimization design method was proposed, which used a design of experiment (DOE) of Latin hypercube sampling (LHS) design combined with a radial basis function model to improve the shape of underwater vehicles. Li et al. [12] used RANS equations and SST $k-\omega$ model in ANSYS Fluent. They proposed a simplified shape optimization (SSO) strategy for blended-wing-body under-water gliders (BBWUGs) by using a Kriging-based constrained global optimization (KCGO) method to optimize the aerofoil shape. And the results showed that the lift-resistance ratio was improved. Zhao et al. [13] used the realisable $k-\varepsilon$ two-layer model to describe the influence of turbulence in STAR-CCM+. Lackenby method was used to modified the main hull of the trawler and NSGA-II algorithm and Sobol + Tsearch algorithm are used to optimize the trawler. The reliability of optimization results was verified by comparing the experimental and numerical results. Wang et al. [14] used RANS equations and SST $k-\omega$ model in ANSYS CFX. The free-form deformation (FFD) parametric method and the surrogate-based optimization (SBO) algorithm were proposed to optimize the hydrofoil shape. Finally, the lift-resistance ratio of the optimized hydrofoil was improved by more than 90%. Vasudev et al. [15] used RANS equations and SST $k-\omega$ model in CFD solver and used genetic algorithm (GA) and CFD solver to optimize the hull shape at a single velocity. Liu et al. [16] used RANS equations and SST $k-\omega$ model in OpenFOAM. The multidisciplinary design optimization (MDO) method is applied to the multiple objective MDO design of the heavier-than-water underwater vehicle (HUV). They also combined the non-dominated sorting genetic algorithms (NSGA-II) and the Kriging model to search the optimal performance of the HUV. Wu et al. [17] used RANS equations in OpenFOAM. An optimization method which combines the lifting line theory and the continuous concomitant method was invented to solve the conflict between shape design and propeller design. The numerical results showed that the AUV resistance was reduced about 17% at rated velocity. In addition to the optimization of traditional hull shapes, new types of structures have also been designed through bionics. For example, an innovative design underwater glider was proposed in [18] which used SST $k-\omega$ model in SolidWorks Flow Simulation and mimicked a whale shark. The results showed that the whale shark-like glider has less resistance, higher lift-resistance ratio and significant gliding capability in practice.

For multivariate problems, it is difficult to accurately establish the connection between input and output parameters in practical engineering. Response surface quadratic model is widely used for analysis and improvement because of its low process complexity and high fitting accuracy. Sun et al. [19] optimized the space utilization and range of AUV by using response surface method (RSM) model and demonstrated the effectiveness of using RSM for shape optimization based on experiments. Liu et al. [20] investigated the strength and stability of carbon fibre composite AUV shell with reinforcement ribs based on finite element analysis

(FEA) and RSM. Kriging is an exact interpolation method that can replace the multiple quadratic regression equations in RSM because of its powerful and flexible properties [21-23]. Kriging-based RSM has higher accuracy and reliability. To obtain the optimal solution, the regression equations analysis of the RSM model is necessary. Guan et al. [24] developed a optimization procedure which integrating a parametric geometric model, a numerical analysis of the total resistance, a RSM model and an evolutionary optimization algorithm to illustrate the effectiveness of the optimization by using a mapping strip. Guan et al. [25] also used the particle swarm optimization (PSO) algorithm and sequential quadratic programming (SQP) algorithm to solve the approximation model established by the second-order RSM and verified the effectiveness of the automatic optimization design method with a 7m unmanned surface vehicle (USV).

In this paper, a small underwater vehicle is designed with the Myring curve as a reference to adsorb the target. Therefore, the hull shape of the small underwater vehicle is controlled by a parametric Myring curve with six design variables. In view of the vehicle's special hull shape, it is necessary to constrain the range of each design variable by CFD so that the optimized hull shape can be found rapidly and accurately. The convergence of the mesh is studied to ensure the correctness of the calculation. A technique integrating Kriging-based RSM and multi-objective optimization algorithm is proposed to optimize the vehicle's design variables to reduce the resistance and increase the volume when moving underwater. The calculation results show that the optimization method is applied to optimize the hull shape of the vehicle effective.

2. Optimization Process

In this paper, SolidWorks and ANSYS are used to optimize the hull shape of a small underwater vehicle. The optimization process is shown in Fig. 2. First, the head and tail parts of the vehicle is built using Myring curve which is controlled by equation. Rotation and stretching are adopted to create the vehicle entity. Changing five input design variables to realize the model reconstruction. Then, the vehicle model is imported into ANSYS Workbench. In geometry module, basin is created, the faces of velocity input and pressure output are determined. The structured mesh is generated in ICEM module and its convergence is verified by studying the first layer height above the vehicle and the number of grid elements. Finally, analytical settings are adjusted and the vehicle resistance is calculated in Fluent module.

After creating these modules, the values of five design variables is changed respectively to calculate and obtain the constraints of each design variable. Then, set the range, name and unit of the input and output variables in the parameter module. The Latin hypercube sampling design is set to obtain a certain number of sample values. Finally, the Kriging-based response surface is established and the goal is to minimize resistance and maximize volume. In optimization, Screening and MOGA are selected to optimize the output variables.

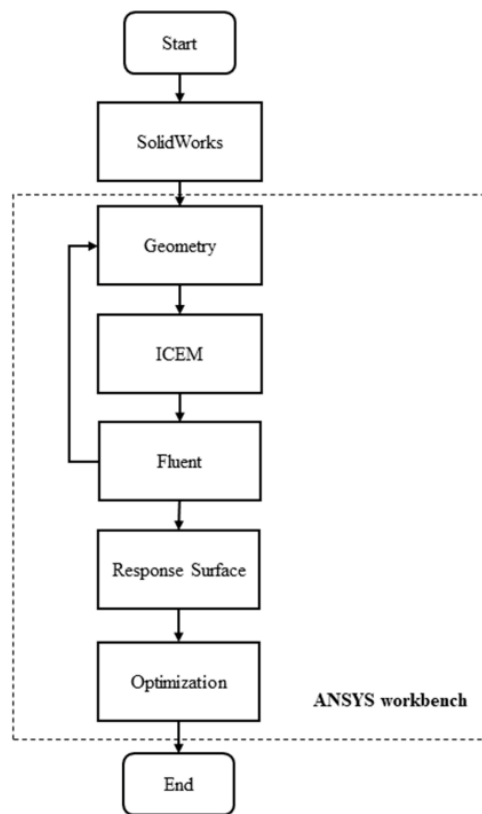


Fig. 1 Optimization process

3. Mechanical Design

3.1 Overall Design

A new small underwater vehicle designed in this paper aims to adsorb the bottom of the ship which sailing on the water. After the vehicle is equipped with the sub-robot, it can corrode and damage the ship, to reduce the combat readiness of enemy ships and further consume the maintenance cost of ships. The overall design of small underwater vehicle is shown in Fig. 1. The body is divided into four parts: adsorption device, sealed pressure-resistant bin, expansion module and propeller. The vehicle is driven by propeller, and the magnet controlled by sensor ejects and adsorbs the target when approaching it.

The design parameters of small underwater vehicle are shown in Table 1. Where d is the maximum diameter of the vehicle, L is the total length of the vehicle, v_m is the maximum navigation velocity of the vehicle, t_m is the minimum navigation time of the vehicle and h_m is the maximum working depth of the vehicle.

Table 1 Small underwater vehicle design parameters

Design parameters	Value
d	90 mm
L	600~800 mm
v_m	2 m/s
t_m	10 min
h_m	60 m

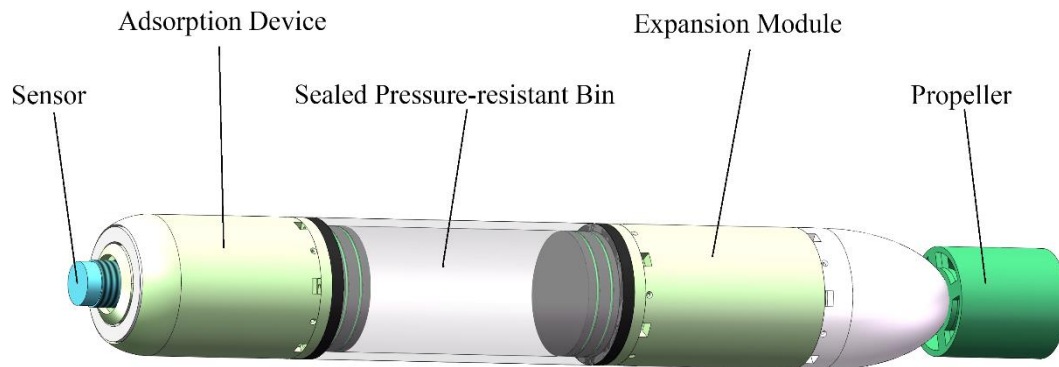


Fig. 2 Overall structural design of small underwater vehicle

3.2 Adsorption Device Design

Considering the influence of the adsorption device on the vehicle resistance, the part of adsorption is hidden in the device. Since the contact surface of the adsorbed target is plane, the magnet surface is selected as plane. The untriggered and triggered states of the annular adsorption device is shown in Fig. 3. The proximity sensor located in the head of the vehicle makes the electromagnet lose its magnetic force so that the magnet is ejected by the spring and adsorb the target when approaching it.

Claw adsorption device is shown in Fig. 4. The adsorption type and working principle are like the annular adsorption device. The claw adsorption device has better hydrodynamic performance compared with the annular adsorption device. Its magnets are evenly distributed on the four claws which are controlled by the electromagnet. Four claws are required to be opened until all magnets are coplanar to achieve the best adsorption effect. At the same cost, the efficiency of claw adsorption device is lower than the annular adsorption device. Therefore, the annular adsorption device is selected in the study.

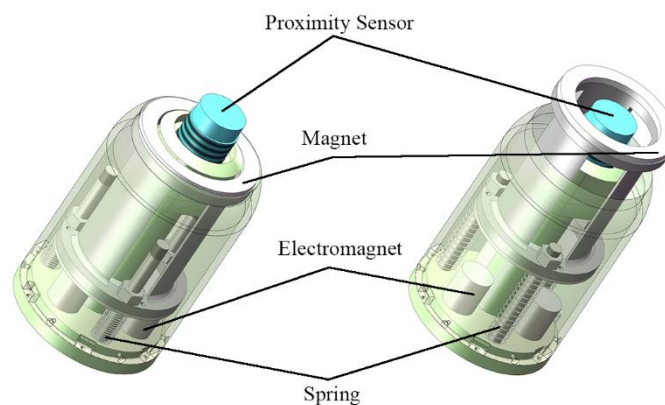


Fig. 3 Annular adsorption module of the vehicle

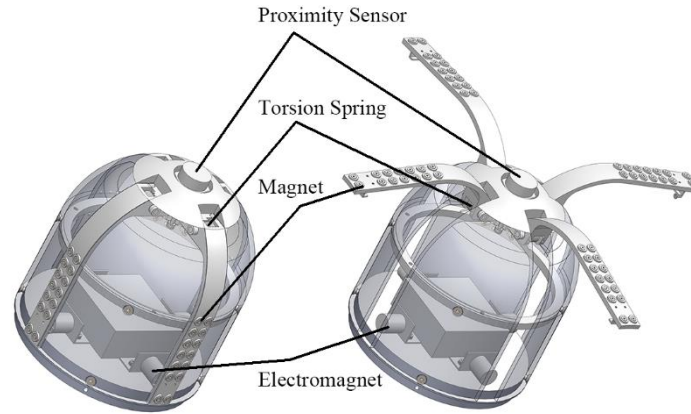


Fig. 4 Claw adsorption module of the vehicle

3.3 Sealed Pressure-Resistant Bin Design

There are some electronic components in sealed pressure-resistant bin, including control circuit board, wires, electronic governor and signal receiver. The sealing ring is selected to seal and prevent the electronic components from being eroded by water. PMMA is selected to make sealed pressure-resistant bin whose geometric model is shown in Fig. 5. The design parameters of sealed pressure-resistant bin are shown in Table 2. Where l_s is the length of bin, d_s is the internal diameter of bin, t_s is the thickness of bin and E is the modulus of elasticity.

Table 2 Sealed pressure-resistant bin design parameters

Parameters	$l_s(\text{mm})$	$d_s(\text{mm})$	$t_s(\text{mm})$	$E(\text{Pa})$
Value	200	80	5	3.16×10^9

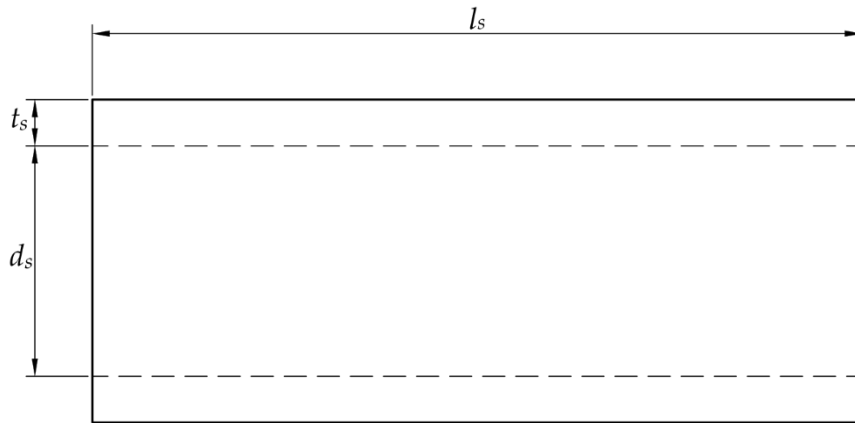


Fig. 5 Geometric model of sealed pressure-resistant bin

The maximum working depth of the vehicle is shown in Table.1. To protect the internal devices, the critical pressure of the vehicle is designed to be greater than the interaction pressure underwater. The critical pressure, P_c , is calculated by Eq 1 which is referenced in [10]

$$P_c = \frac{2.6E \left(\frac{t_s}{d_s} \right)^{\frac{5}{2}}}{\frac{l_s}{d_s} - 0.45 \left(\frac{t_s}{d_s} \right)^{\frac{1}{2}}} \quad (1)$$

P_c is about 3.39 MPa. The interaction pressure mainly comes from the pressure of water, P .

$$P = \rho gh_m \quad (2)$$

where ρ is the density of water and g is gravity. P is calculated at about 0.62 MPa. It can be seen from the results that P_c is greater than P .

3.4 Expansion Module Design

As shown in Fig. 6, there is a cavity with diameter of 80mm and length of 100mm in the expansion module. The expansion module is used to store a sub-robot which is ejected from the vehicle and adsorbs the ship to corrode and damage the target. The length of the sub-robot is 65mm, and the maximum diameter is 30mm. A door opening mechanism is designed on the module surface. The length of the door is 85mm and the width is 50mm. Considering the space size of the module, the door opening mechanism is simplified. A torsion spring is installed at the connection between the door and the module. Choosing the electromagnet likes adsorption device to control the state of the door. The door is opened by the torsion spring and the sub-robot is ejected when the electromagnetic switch triggered.

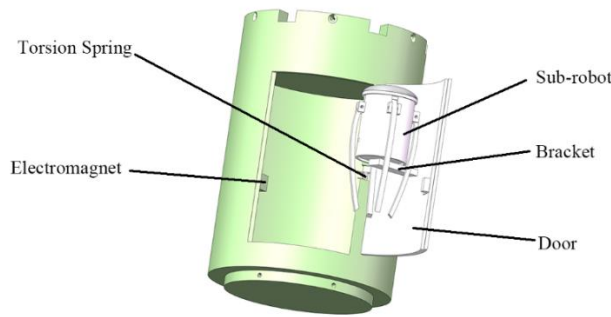


Fig. 6 Expansion module of small underwater vehicle

3.5 Hull Shape Design

The hull shape of underwater vehicle is usually designed to be spherical, ellipsoidal or cylindrical. The head and tail of underwater vehicle are a combination of these shapes. We need to install a functional mechanism in the vehicle head and a propeller in the tail. Therefore, the vehicle's space utilization and hydrodynamic performance should be considered at the same time in the design. In particular, the improvement of hydrodynamic performance is the focus of our attention.

In general, the hydrodynamic performance of the underwater vehicle depends on its hull shape. Myring and NURBS are often used in shape design [26, 27]. In the unmanned vehicles, the rotary Myring curve is most used, such as Remus [28]. In this paper, Myring curve is used to build the profile of small underwater vehicle.

As shown in Fig. 7, it is a schematic diagram of Myring curve with six design variables. The head curve equation of the vehicle is:

$$y(x) = \frac{d \left(1 - \left(\frac{x-a}{a} \right)^2 \right)^{\frac{1}{n}}}{2} \quad (3)$$

where d is the maximum diameter of the vehicle, a is the length of the head and n is the dimensionless variable, which controls the profile of the head. Especially, the larger n is, the more circular the head is. The equation of the vehicle tail curve is given as follows:

$$y(x) = \frac{d}{2} - \left(\frac{3d}{2c^2} - \frac{\tan \theta}{c} \right) (x-a-b)^2 + \left(\frac{d}{c^3} - \frac{\tan \theta}{c^2} \right) (x-a-b)^3 \quad (4)$$

where b is the length of the middle, c is the length of the tail and θ is the tail semi-angle, which controls the profile of the tail. Similarly, the larger the θ is, the rounder the tail is.

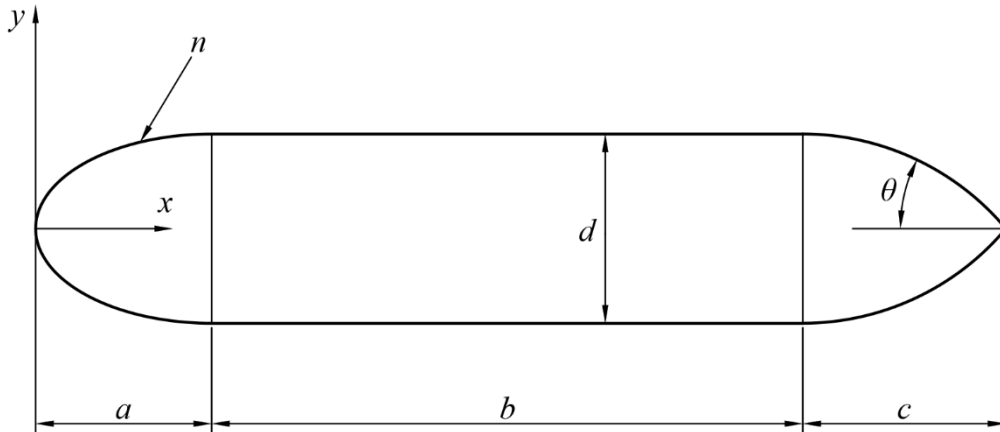


Fig. 7 Myring model

Fig. 8 shows the equivalent research model of the designed vehicle. The vehicle is parametrically modelled by using SolidWorks and the head and tail profiles of the vehicle are controlled by curve equations. Where d_m is the diameter of the magnet. According to the size of the selected magnet, it is ensured that $d_m=76$ mm.

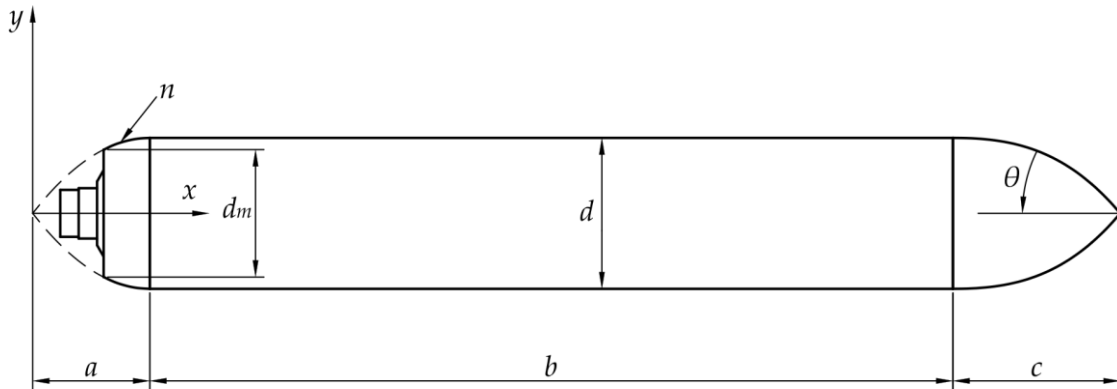


Fig. 8 Vehicle equivalent model

4. CFD Analysis

As shown in Fig. 9, the initial model of the vehicle is established in SolidWorks, and a is 70 mm, n is 1, b is 480 mm, c is 100 mm, θ is 50° , d is 90 mm. The volume of the vehicle is 0.00358 m^3 by measuring.

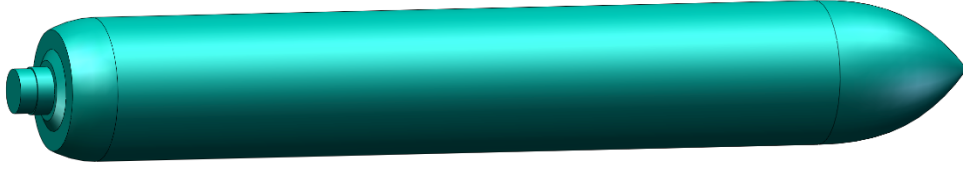


Fig. 9 Initial model of the vehicle

4.1 Controlling Equation and Computation Domain

The commercial software ANSYS Fluent 2021 R1 is selected as the CFD solver. The underwater environment is regarded as an incompressible fluid and is a turbulent field. The simulation takes Reynolds-averaged Navier-stokes (RANS) equations as the controlling equation. The author of [15] compares the errors of resistance coefficients of different turbulence models, taking SST $k-\omega$ turbulence model has least errors. The RANS have an advantage of being computationally efficient. Its average mass and momentum transfer equations are as follows [29]:

$$\frac{\delta \rho}{\delta t} + \frac{\delta}{\delta x_i}(\rho u_i) = 0 \quad (5)$$

$$\frac{\delta}{\delta t}(\rho u_i) + \frac{\delta y}{\delta x_j}(\rho u_i u_j) = \frac{\delta p}{\delta x_j} + \frac{\delta}{\delta x_j} \left(\mu \frac{\delta u_i}{\delta x_j} - \overline{\rho u_i' u_j'} \right) + S_j \quad (6)$$

where u_i is the time-averaged value of the velocity component, t is the time, p is the time-averaged value of the pressure, ρ is the fluid density, μ is the dynamic viscosity coefficient, $\overline{\rho u_i' u_j'}$ is the Reynolds stress term, and S_j is the generalized source term of the momentum equation.

Computation domain is established in Fig. 10. Considering the development of the downstream wake. The domain with length of $6L$, width of $10d$ and height of $10d$ is built, where turbulence can be considered. The vehicle is placed at $2L$ to the left boundary and $4L$ to the right boundary. The left wall is set as velocity inlet with a fixed horizontal velocity value and the right wall is set as pressure outlet.

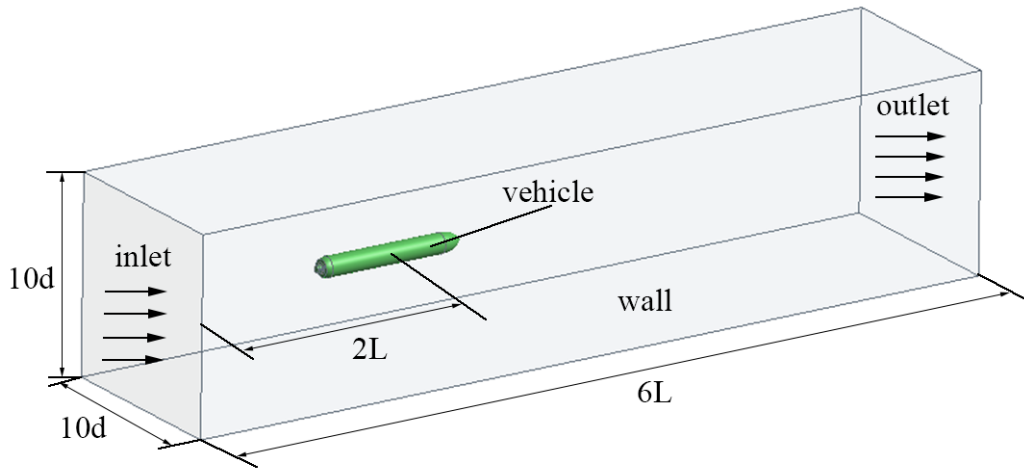


Fig. 10 Computation domain

4.2 Grid Convergence Study for Resistance

A structured mesh is generated for CFD simulation using ANSYS ICEM. The detailed grid elements of the vehicle are shown in Fig. 11. The grids density is high around the vehicle. The y^+ for the first layer of the elements from the vehicle is around 1. This y^+ is suggested for the use of the SST $k-\omega$ turbulence model [30]. The kinematic viscosity, ν_k , can be calculated by

$$\nu_k = \frac{\mu}{\rho} \quad (7)$$

where μ is the dynamic viscosity of the fluid. The Reynolds number, Re , is calculated as

$$Re = \frac{vd}{\nu_k} \quad (8)$$

where v is the velocity of the vehicle. The skin friction coefficient on the vehicle is

$$C_f = 0.058Re^{-0.2} \quad (9)$$

Wall shear stress, τ_w , is given by

$$\tau_w = \frac{1}{2} C_f \rho v^2 \quad (10)$$

Friction velocity, U_τ , is calculated by

$$U_\tau = \frac{\tau_w}{\rho} \quad (11)$$

And the first layer height above the vehicle, y , is calculated by

$$y = \frac{y^+ \nu_k}{U_\tau} \quad (12)$$

In all calculation, a value of $y=0.01$ mm is taken to satisfy $y^+=1$.

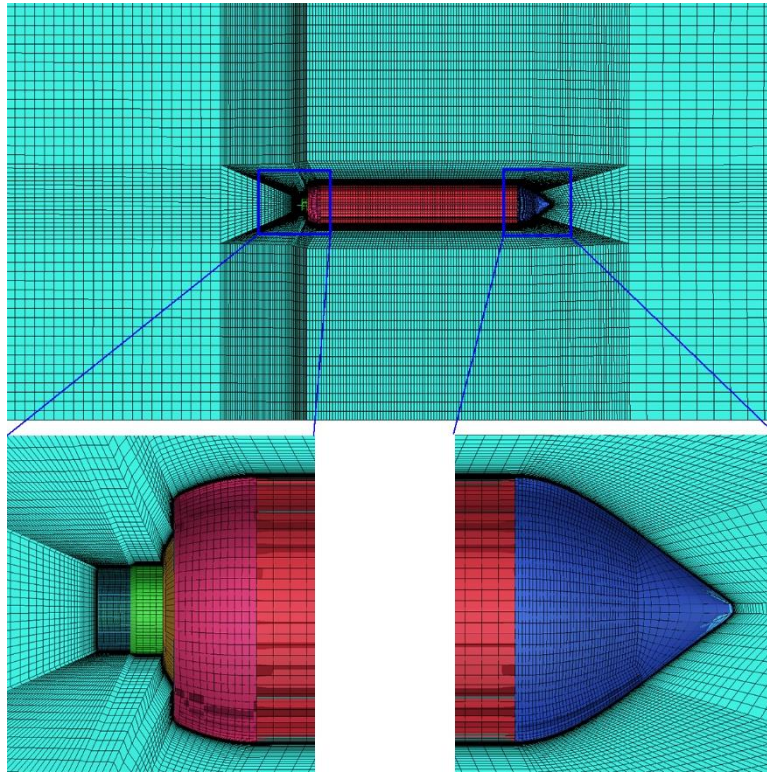


Fig. 11 Mesh details

The numerical results can be accurate if they are not affected by the number of grid elements. As shown in Table 3, there are three different mesh resolutions to evaluate the influence of the number of grid elements on the vehicle resistance. The fine mesh with 5.0 million cells, the medium mesh with 2.7 million cells and the coarse mesh with 0.9 million cells are calculated at $v=2$ m/s. It can be seen from the table that the results of the fine mesh and the medium mesh are given approximately. Therefore, the vehicle resistance will not change a lot by increasing the number of grid elements. Considering the efficiency of calculation, the mesh with 2.7 million cells is selected for the following calculation.

Table 3 Results of resistance for mesh verification

Number of grid elements (million)	Vehicle resistance (N)
0.9	2.980
2.7	2.940
5.0	2.936

4.3 Numerical Calculation

The vehicle subjected resistance is normally divided into pressure resistance, viscous resistance and wave making resistance [31]. The wave making resistance is so small that it can be ignored when the sailing depth is more than one-third of the vehicle length. Therefore, only the pressure resistance and viscous resistance are considered in this paper.

In simulation, the vehicle is analysed for resistance at the depth of 60 m and $v=0.5$ m/s, 1 m/s, 1.5 m/s and 2 m/s respectively. The resistance conditions at different velocities are shown in Table 4. Where F_t is the total resistance of the vehicle in the water, F_p is the pressure resistance and F_v is the viscous resistance. As shown in Fig. 12, it can be seen that F_p is larger than F_v and F_t is equal to the sum of F_v and F_p when the vehicle navigates underwater.

The main reason why F_p is much larger than F_v is that the vehicle head lacks a streamlined part for the design of the sensor and the adsorption module. The curve shows that F_t , F_v and F_p all increase with the raise of the vehicle's velocity and F_t is proportional to the quadratic of the velocity. F_t and F_p change significantly with the increase of velocity and F_v is little affected by velocity. The static pressure distribution image is shown in Fig. 13.

Table 4 Resistance of the vehicle at different velocities

$v(\text{m/s})$	0.5	1.0	1.5	2.0
$F_t(\text{N})$	0.228	0.811	1.698	2.940
$F_p(\text{N})$	0.123	0.451	0.996	1.767
$F_v(\text{N})$	0.105	0.360	0.702	1.173

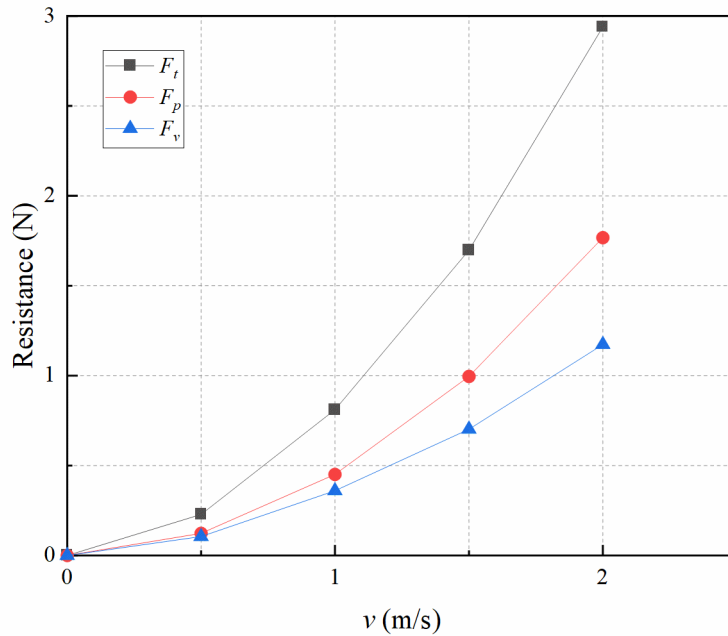


Fig. 12 Relationship between v and resistance

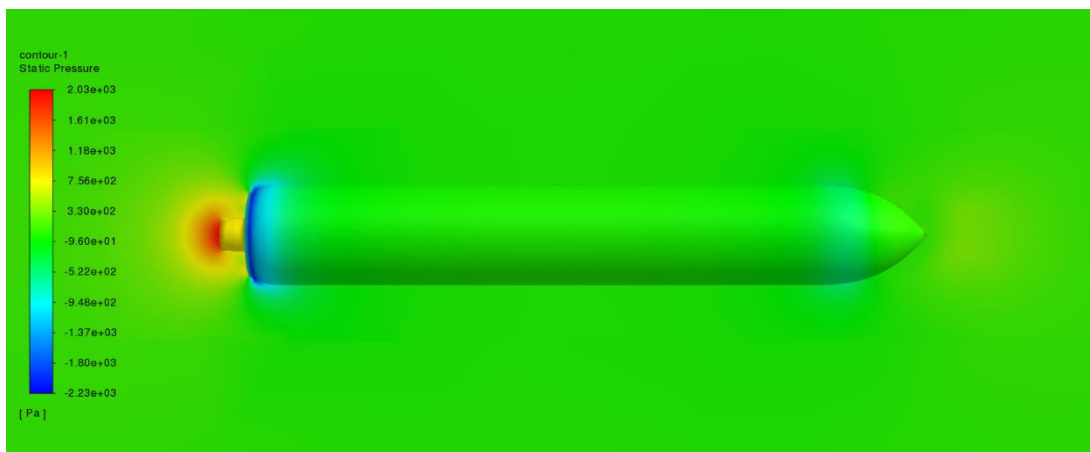
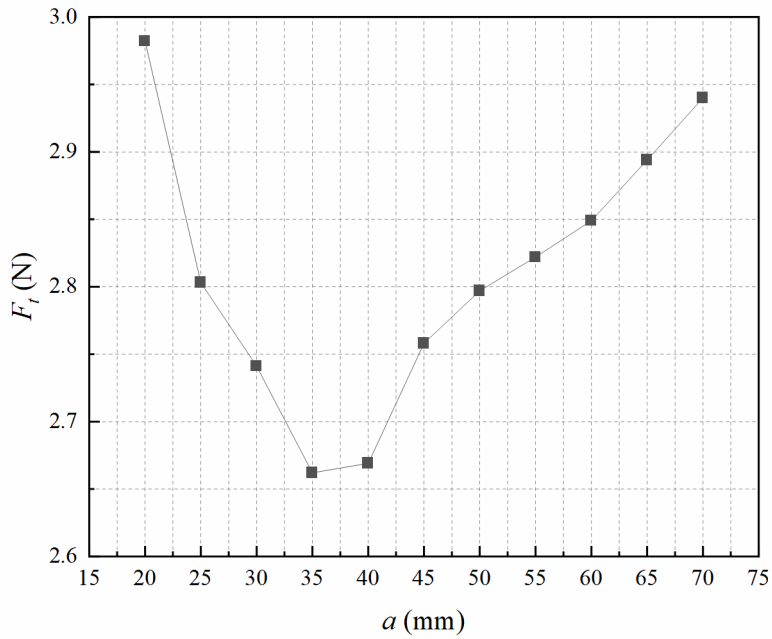


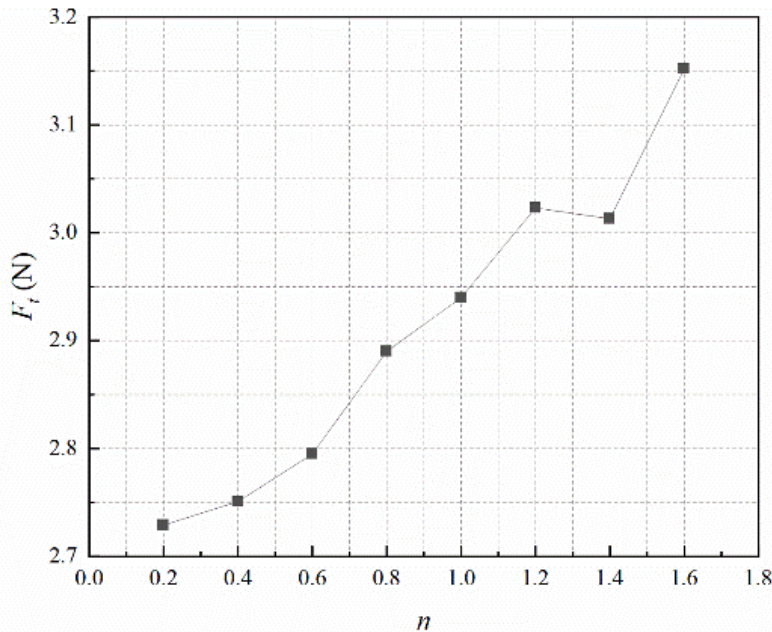
Fig. 13 The static pressure distribution of the vehicle at 2 m/s

To investigate the effect of each design variable on the resistance, the variables a , n , b , c , and θ are used as variables to perform CFD of the vehicle at 2 m/s respectively. The relationship between F_t and design variables of the vehicle is shown in Fig. 14. It can be seen from the image that each variable affects F_t . F_t decreases rapidly when a increases between 20 mm and 35 mm. F_t shows a tendency to increase when a increases between 35 mm and 70

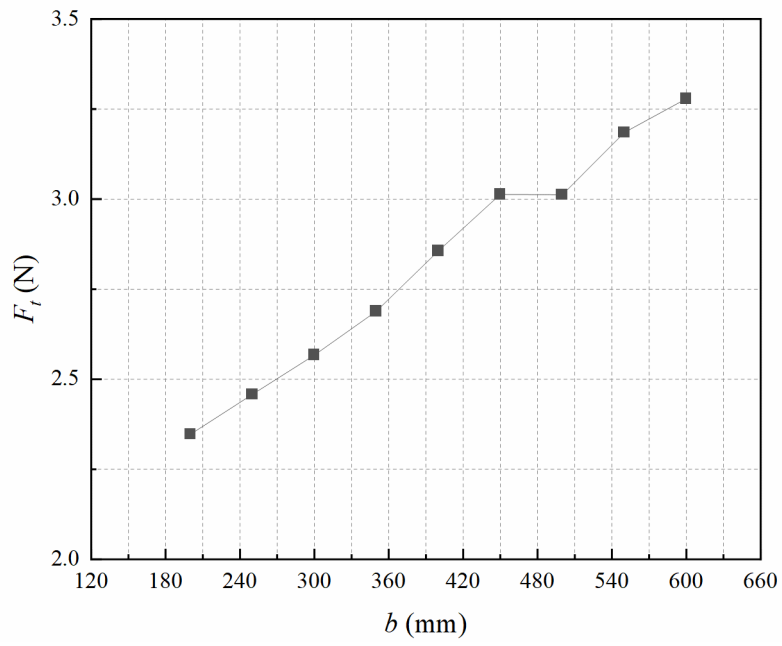
mm. Therefore, the range of a is taken from 25 mm to 55 mm. F_t increases when n increases between 0.2 and 1.6. Therefore, the range of n is taken from 0.2 to 1.2. F_t grows linearly when b increases. Obviously, the smaller b is, the F_t smaller is. However, most electronic components are stored in the middle part of the vehicle and b should be taken to satisfy the constraint of L shown in Table 1. Therefore, b is taken from 400 mm to 550 mm. F_t decreases rapidly when c increases between 30 mm and 50 mm. Then, F_t fluctuates when c increases between 50 mm and 130 mm. The minimum F_t is located in $c=80$ mm. Therefore, the range of c is taken from 50 mm to 120 mm. The relationship between F_t and θ is similar to the relationship between F_t and c . The range of θ is taken from 10° to 50° to obtain an accurate θ under this trend.



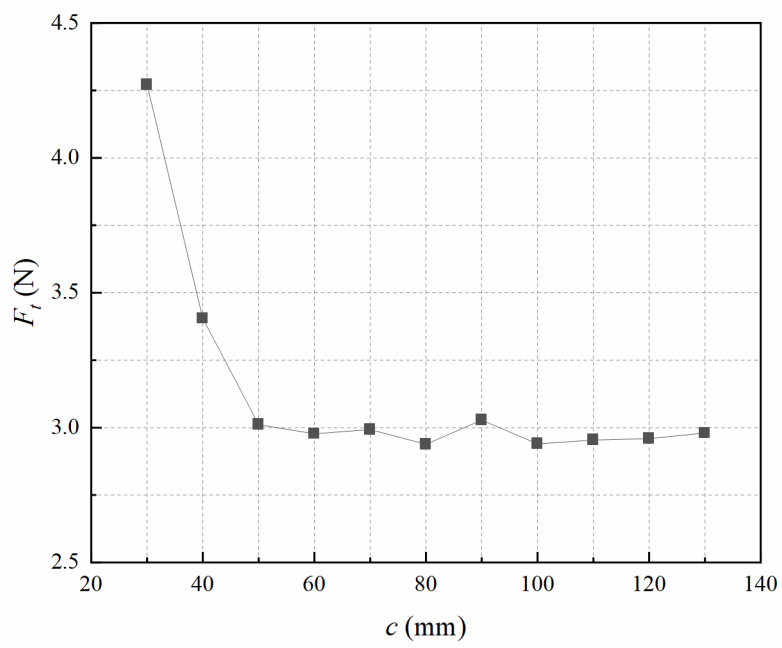
(a)



(b)



(c)



(d)

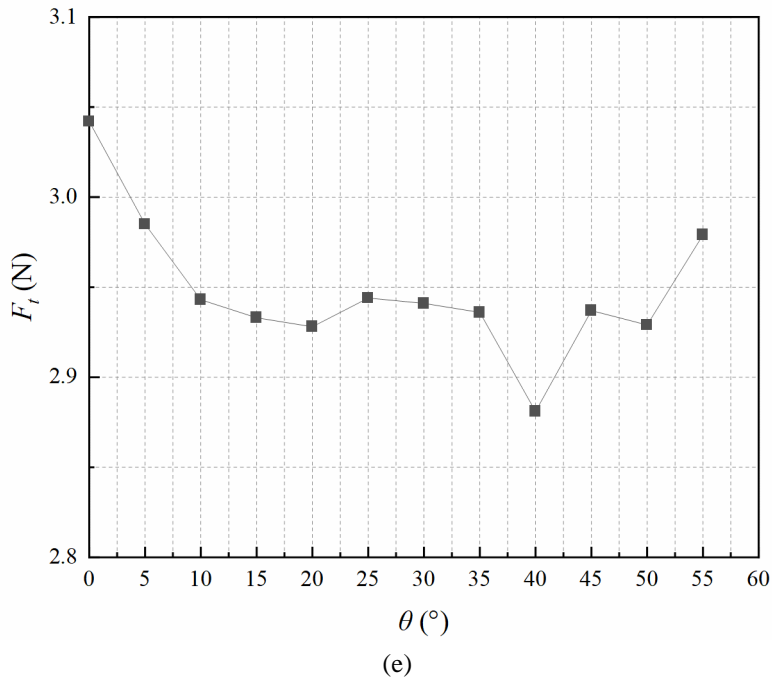


Fig. 14 The relationship between design variables and F_t : (a) $a-F_t$, (b) $n-F_t$, (c) $b-F_t$, (d) $c-F_t$, (e) $\theta-F_t$

5. Optimization

In the previous section, the discrete analysis on different design variables of the vehicle is performed to estimate the resistance of the vehicle and determines the range of design variables. In this section, Workbench 2021 R1 is applied to connect the Fluent module and Response Surface Optimization module to build an automated modelling analysis. A Kriging-based response surface method is used to build a mathematical model and the optimal hull shape is found by Screening and MOGA used in [20, 32]. The Screening optimization method uses a simple approach based on sampling and sorting. It supports multiple objectives and constraints as well as all types of input parameters. The MOGA method is a variant of the popular NSGA-II based on controlled elitism concepts. It supports multiple objectives and constraints and aims at finding the global optimum.

5.1 Kriging-Based Response Surface Method

Response surface method (RSM) is a statistical method to solve multivariate problems by using reasonable experimental design methods and obtaining certain data through experiments. It uses a multiple quadratic regression equation to fit the functional relationship between factors and response values and to seek the optimal variables.

There are various experimental designs which can perform response surface analysis such as Latin hypercube sampling (LHS) design, central composite design (CCD) and box-behnken design (BBD) [33, 34]. In this paper, the design variables are range-based and LHS design is chosen as an experimental design method.

LHS design is used to generate random values of each design variable and to make each variable appear only once in any row or column of the experimental design matrix. Therefore, the randomized LHS design method is used to design a more homogeneous and complete area which is covered with a minimum number of sample points. LHS design method is suitable for the Kriging-based RSM which is an interpolation method. CCD and BBD design methods are valid for traditional polynomial based RSM.

The Kriging method is a spatial interpolation method based on random positions. Its theoretical approach was proposed in 1970 and was later applied to the engineering discipline. The Kriging model has high prediction accuracy and good nonlinear fitting ability and can replace the second-order polynomial as a meta model to obtain higher accuracy of the response surface. The Kriging model expression is [35]:

$$y(X) = F(\hat{\beta}, X) + Z(X) \quad (13)$$

where X is the input variable set, $y(X)$ is the predicted response value, $F(\hat{\beta}, X)$ is the regression model, $\hat{\beta}$ is the regression coefficient and $Z(X)$ is the measure of the deviations from the regression model. The covariance of $Z(X)$:

$$Cov[Z(x_i), Z(x_j)] = \sigma^2 R(x_i, x_j) \quad (14)$$

where $R(x_i, x_j)$ is correlation function between any two values in the input variables, and its expression is:

$$R(x_i, x_j) = \exp\left[-\sum_{k=1}^K \theta_k (x_i^k - x_j^k)^2\right] \quad (15)$$

where θ_k which is used to estimate the correlation relationship between the test points is the parameter of the correlation function. The distance between two points is changed by changing the value of θ_k , which changes the correlation between two points and can generate a smoother surface.

In Eq 13, β is estimated using Eq 16:

$$\hat{\beta} = (f^T R^{-1} f)^{-1} f^T R^{-1} y \quad (16)$$

where f is a column vector, R is the correlation matrix of training data and y is a row vector. The output values of final design points in the Kriging-based RSM is:

$$\hat{y}(x) = \hat{\beta} + r^T(x) R^{-1} (y - f\hat{\beta}) \quad (17)$$

where $r(x)$ is the correlation vector between the untried x and the sampled points.

Five design variables which control the vehicle's hull shape are analysed in previous section. Considering the problem of variables interaction occurs in the stage of model reconstruction, four design variables a , n , b , c , and θ are introduced to Kriging-based RSM.

5.2 Response Surface Optimization

The Kriging-based response surface of the vehicle hull shape is established and optimized. The developed response surface model is used to analyse any two input variables effects on two output variables by three-dimensional response surface. The relationship between output variables and input design variables is shown in Table 5 by automated modelling analysis. The generated Kriging model is verified with ten sample points different from the set of designs used for generation. The goodness of fit of response surface is shown in Fig. 15. It can be seen from the fitness image that the verification points for V are distributed on the midline and the verification points for F_t are distributed compactly on both sides of the midline. The root mean square error of V is 2.749E-06 and the root mean square error of F_t is 0.0263. The response surface established in ANSYS Workbench is shown in Fig.

16. It can be seen from the image that b and c have a more apparent effect on V , a and n have a more apparent effect on F_t . These conclusions are consistent with ANSYS Workbench sensitivity analysis results, as shown in Fig.17.

We determine the optimization strategy and establish a multi-objective optimization model. F_t is minimized and V is maximized. Then, the model is solved by Screening and MOGA. The optimization problem formulation is

$$\left\{ \begin{array}{l} \min F_t \\ \max V \\ 25 \leq a \leq 55 \\ 0.2 \leq n \leq 1.2 \\ 400 \leq b \leq 550 \\ 50 \leq c \leq 120 \\ 10 \leq \theta \leq 50 \end{array} \right. \quad (18)$$

In this paper, Screening and MOGA are used to optimize the hull shape of the vehicle. The objective functions are to maximize V and to minimize F_t . Fig.18 shows the obtained Pareto front for V and F_t . Each red point represents a Pareto optimal solution and all red points constitute the Pareto front. F_t plays more important role in optimization. Therefore, the objective importance of F_t is set higher than V in decision support process. By this decision technique, five candidate points (C1, C2, C3, C4 and C5) are selected from Fig.18 and the values of the objective functions are shown in Table 6 and Table 7. The candidate points are calculated by CFD to verify the effectiveness of optimization results. As the results shown in Table 6 and Table 7, the maximum errors of V and F_t are 0.11% and 1.54% using Screening, and they are 0.19% and 1.48% using MOGA, which is acceptable in the optimization. As shown in Table 8, compared with the initial hull shape of the vehicle, V increased 1.40% and F_t decreased 8.98% using Screening and V increased 3.07% and F_t 9.52% decreased using MOGA. Both optimization methods can obviously improve the hull shape of the vehicle and the hull shape of the vehicle in MOGA is superior to in Screening. Therefore, the design variables are round to $a=45$ mm, $n=0.8$, $b=506$ mm, $c=96$ mm and $\theta=49^\circ$ based on the principle of proximity. The generated optimal model is shown in Fig. 19.

Table 5 Test sample sites

Number	a (mm)	n	b (mm)	c (mm)	θ ($^\circ$)	V (m^3)	F_t (N)
1	36.1	0.27	545.5	54.9	21.6	0.00367	3.454
2	41.5	0.85	461.5	61.9	12.0	0.00320	2.754
3	25.9	1.05	413.5	87.1	25.6	0.00295	2.629
4	38.5	0.79	542.5	115.1	19.2	0.00387	2.865
5	27.1	0.43	425.5	99.7	40.0	0.00310	3.016
6	52.9	0.51	491.5	53.5	44.8	0.00339	2.768
7	37.9	0.93	536.5	77.3	36.8	0.00374	2.814
8	52.3	0.81	401.5	82.9	16.8	0.00290	2.567
9	30.7	0.57	446.5	96.9	26.4	0.00319	2.772
10	28.9	1.19	416.5	89.9	40.8	0.00303	2.542
11	33.1	0.21	422.5	71.7	24	0.00293	3.280

12	28.3	0.69	467.5	57.7	44.0	0.00322	2.881
13	35.5	0.65	440.5	70.3	42.4	0.00310	2.629
14	43.3	1.13	455.5	94.1	30.4	0.00330	2.675
15	32.5	0.39	548.5	109.5	12.8	0.00384	3.144
16	48.7	0.99	524.5	68.9	17.6	0.00364	2.871
17	47.5	0.71	428.5	56.3	32.8	0.00299	2.662
18	40.9	1.15	518.5	101.1	47.2	0.00379	2.777
19	27.7	0.61	485.5	64.7	16.0	0.00332	3.047
20	26.5	1.17	497.5	102.5	15.2	0.00352	2.714
21	34.9	0.83	473.5	108.1	23.2	0.00341	2.687
22	49.3	0.37	521.5	116.5	29.6	0.00376	2.797
23	53.5	1.07	506.5	95.5	11.2	0.00361	2.914
24	29.5	0.33	458.5	67.5	13.6	0.00315	3.145
25	45.1	0.73	419.5	119.3	32.0	0.00316	2.542
26	40.3	0.59	482.5	80.1	37.6	0.00340	2.731
27	46.9	0.55	509.5	73.1	36.0	0.00355	2.798
28	42.7	0.35	443.5	98.3	49.6	0.00327	2.728
29	54.1	0.53	410.5	106.7	28.8	0.00304	2.542
30	33.7	0.97	479.5	66.1	24.8	0.00332	2.715
31	45.7	1.03	437.5	105.3	48.0	0.00331	2.588
32	48.1	0.95	407.5	50.7	22.4	0.00285	2.877
33	36.7	0.63	494.5	74.5	34.4	0.00345	2.759
34	49.9	0.91	515.5	52.1	39.2	0.00355	2.904
35	34.3	1.01	488.5	112.3	35.2	0.00357	2.679
36	31.3	0.29	431.5	85.7	38.4	0.00307	3.080
37	51.7	0.75	476.5	63.3	43.2	0.00334	2.752
38	51.1	0.45	512.5	103.9	45.6	0.00374	2.800
39	39.7	0.23	470.5	110.9	18.4	0.00336	3.034
40	54.7	1.11	500.5	88.5	10.4	0.00356	2.893
41	39.1	0.47	452.5	78.7	20.8	0.00317	2.700
42	37.3	1.09	449.5	59.1	41.6	0.00314	2.703
43	43.9	0.31	434.5	84.3	14.4	0.00306	2.706
44	30.1	0.49	527.5	75.9	31.2	0.00364	3.073
45	46.3	0.41	539.5	91.3	48.8	0.00385	2.808
46	44.5	0.87	533.5	113.7	46.4	0.00394	2.888
47	50.5	0.25	464.5	81.5	20.0	0.00325	2.764
48	42.1	0.67	404.5	117.9	27.2	0.00303	2.504
49	31.9	0.89	530.5	60.5	28.0	0.00362	2.889
50	25.3	0.77	503.5	92.7	33.6	0.00355	2.984

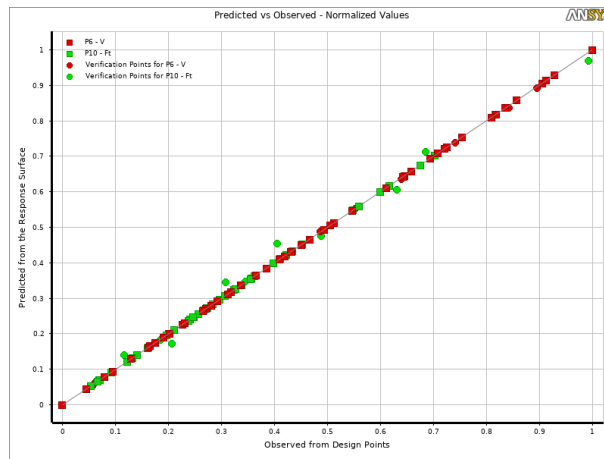


Fig. 15 The goodness of fit of response surface

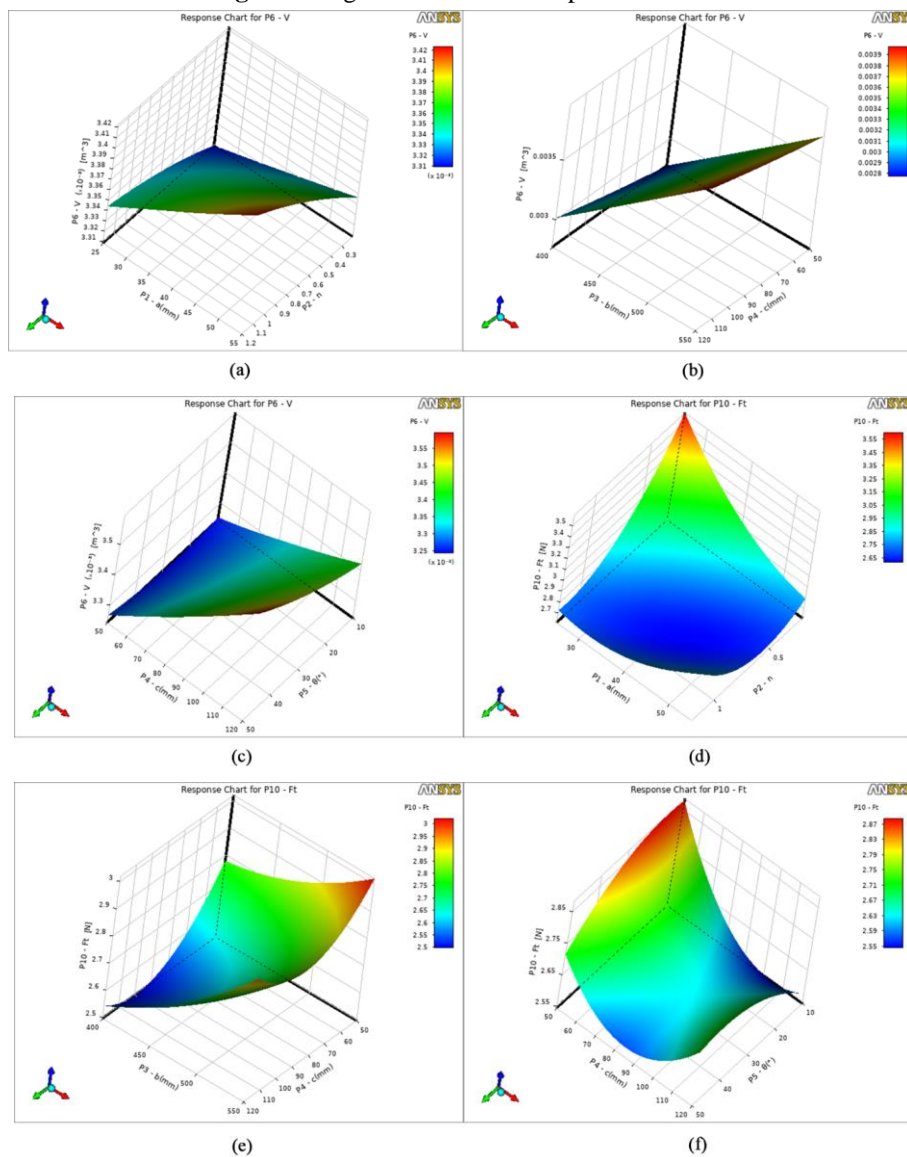


Fig. 16 Response surface model: (a) $a-n-V$, (b) $b-c-V$, (c) $c-\theta-V$, (d) $a-n-F_t$, (e) $b-c-F_t$, (f) $c-\theta-F_t$

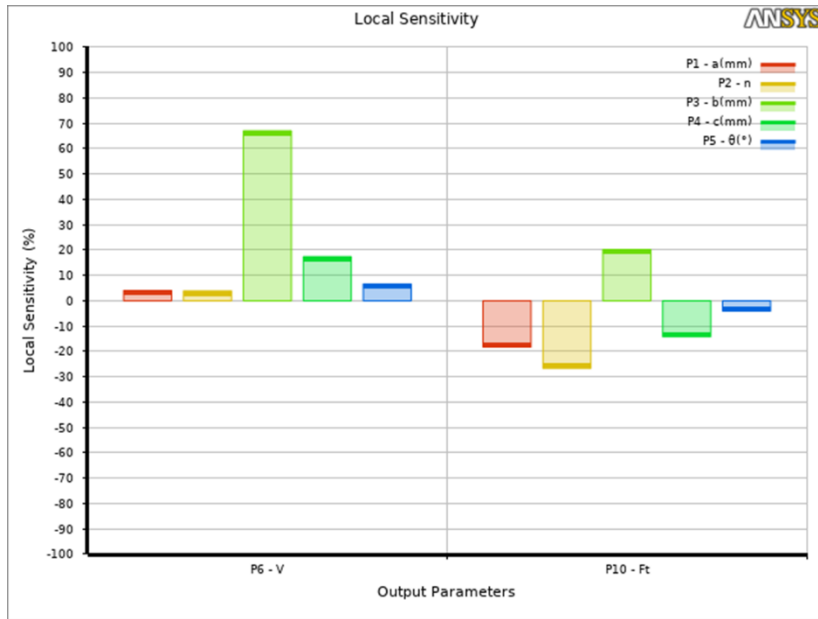
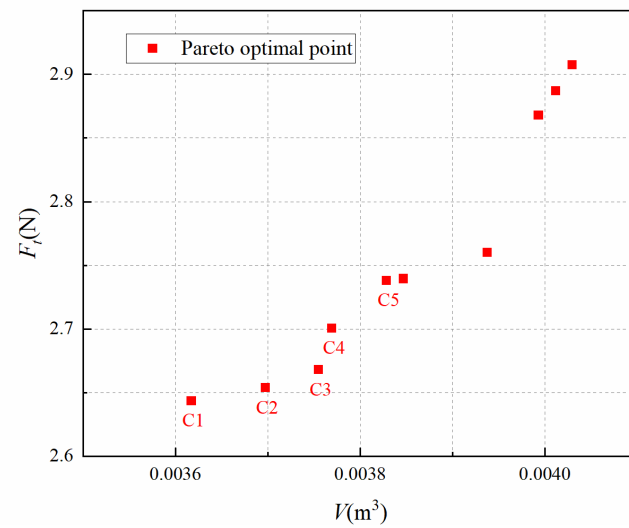
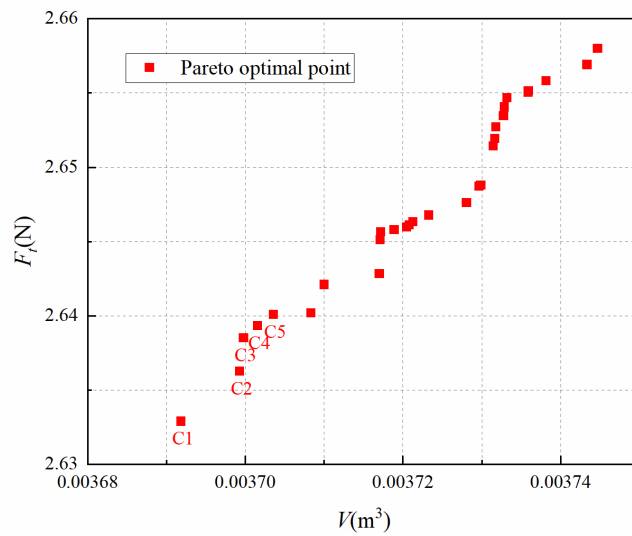


Fig. 17 Variables sensitivity



(a)



(b)

Fig.18 Pareto front with different method: (a) Screening method, (b) MOGA method

Table 6 Comparison of predicted and numerical results for Screening method

	$a(\text{mm})$	n	$b(\text{mm})$	$c(\text{mm})$	$\theta(^{\circ})$	$V(\text{m}^3)$	$F_t(\text{N})$
C1	46.3	0.73	499.2	96.8	42.8	0.003637	2.644
Verified point						0.003633	2.676
Predicted error						0.11%	1.21%
C2	50.7	0.68	511.6	90.0	49.1	0.003697	2.654
Verified point						0.003693	2.687
Predicted error						0.11%	1.24%
C3	49.3	0.72	515.1	97.1	49.5	0.003755	2.668
Verified point						0.003755	2.709
Predicted error						0%	1.54%
C4	53.2	0.66	519.3	94.8	48.3	0.003770	2.701
Verified point						0.003766	2.737
Predicted error						0.11%	1.33%
C5	49.4	0.63	523.2	106.1	46.3	0.003829	2.738
Verified point						0.003829	2.779
Predicted error						0%	1.50%

Table 7 Comparison of predicted and numerical results for MOGA method

	$a(\text{mm})$	n	$b(\text{mm})$	$c(\text{mm})$	$\theta(^{\circ})$	$V(\text{m}^3)$	$F_t(\text{N})$
C1	44.9	0.77	506.4	96.3	49.4	0.003692	2.633
Verified point						0.003692	2.660
Predicted error						0%	1.03%
C2	44.8	0.77	507.7	96.1	49.8	0.003699	2.636
Verified point						0.003699	2.668
Predicted error						0%	1.21%
C3	45.8	0.79	507.3	96.4	49.6	0.003700	2.639
Verified point						0.003693	2.678
Predicted error						0.19%	1.48%
C4	44.0	0.78	508.0	96.5	49.8	0.003702	2.640
Verified point						0.003702	2.670
Predicted error						0%	1.14%
C5	45.8	0.76	505.3	99.8	49.7	0.003706	2.641
Verified point						0.003706	2.678
Predicted error						0%	1.40%

Table 8 Comparison of initial and optimized results

	$a(\text{mm})$	n	$b(\text{mm})$	$c(\text{mm})$	$\theta(^{\circ})$	$V(\text{m}^3)$	Rate(%)	$F_t(\text{N})$	Rate(%)
Origin	70.0	1.00	480.0	100.0	50.0	0.00358		2.940	
Screening	46.3	0.73	499.2	96.8	42.8	0.00363	1.40	2.676	8.98
MOGA	44.9	0.77	506.4	96.3	49.4	0.00369	3.07	2.660	9.52

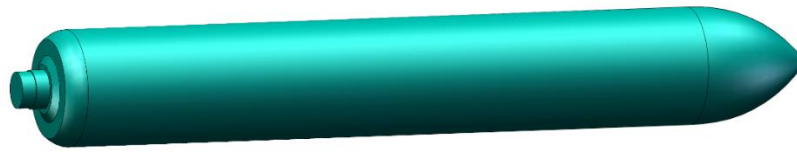


Fig. 19 Optimal model of the vehicle

6. Conclusion

A hull shape optimization design of a small underwater vehicle which is used to adsorb targets is carried out with regard to minimizing the resistance and maximizing the volume in this paper. Firstly, Myring curve with six design variables is used to control the vehicle profile. Then, the value range of design variables and resistance are calculated by CFD. What's more, a Kriging-based RSM model which can predict the resistance and volume is established to optimize the hull shape of the vehicle. Multi-objective optimization algorithm is proposed to find the optimal hull shape:

1. The small underwater vehicle is parametrically modelled using the Myring type as a reference and the profile of the vehicle is controlled by six different variables. This Myring curve can provide a reference for the shape design and optimization of underwater vehicles in the future.
2. The vehicle requires separate functional modules in the head, so the range of each variable based on experience may not meet the design criteria. Therefore, it is important for the optimization that the influence of each variable on the resistance is analysed by using the control variable method to obtain the range of each variable.
3. Through solving the established Kriging-based RSM model using MOGA, the hull shape of the vehicle is optimized obviously compared with initial model.

The Kriging-based RSM model proposed in this paper solves the multivariate consistency constraint and decoupling problems in the overall optimization of small underwater vehicle, and provides a theoretical basis and technical support for the design optimization of similar underwater vehicles.

7. Acknowledgments

This work was supported by the National Natural Science Foundation of China [Grant number 52071102].

REFERENCES

- [1] Hall, J. K., 2006. GEBCO Centennial Special Issue - Charting the secret world of the ocean floor: the GEBCO project 1903-2003. *Marine Geophysical Research*, 27, 1-5. <https://doi.org/10.1007/s11001-006-8181-4>
- [2] Javaid, M. Y., Ovinis, M., Nagarajan, T. and Hashim, F. B. M., 2014. Underwater Gliders: A Review. *4th International Conference on Production, Energy and Reliability (ICER)*, Kuala Lumpur, MALAYSIA. <https://doi.org/10.1051/mateconf/20141302020>

- [3] Shukla, A. and Karki, H., 2016. Application of robotics in offshore oil and gas industry-A review Part II. *Robotics and Autonomous Systems*, 75, 508-524. <https://doi.org/10.1016/j.robot.2015.09.013>
- [4] Li, J.-l., Wang, X.-j., Wang, P., Dong, H.-c. and Chen, C.-h., 2021. Shape Optimization for A Conventional Underwater Glider to Decrease Average Periodic Resistance. *China Ocean Engineering*, 35, 724-735. <https://doi.org/10.1007/s13344-021-0064-6>
- [5] Cole, J. A., Loubimov, G. and Kinzel, M., 2021. Comparison of computational methods for hydrodynamic performance prediction of oscillating marine propulsors. *Ocean Engineering*, 242. <https://doi.org/10.1016/j.oceaneng.2021.110002>
- [6] Du, P., Huang, S. H., Yang, W., Wang, Y., Wang, Z., Hu, R. and Chen, Y., 2022. Design of a Disc-Shaped Autonomous Underwater Helicopter with Stable Fins. *Journal of Marine Science and Engineering*, 10. <https://doi.org/10.3390/jmse10010067>
- [7] Fan, S.-s., Ci, X.-h., Bose, N. and Cheng, X., 2022. Structural and Operational Optimization of A Flapping Fin Used as A Self-Propulsor for AUV Propulsion. *China Ocean Engineering*, 36, 86-99. <https://doi.org/10.1007/s13344-022-0007-x>
- [8] Kilavuz, A., Ozgoren, M., Durhasan, T., Sahin, B., Kavurmacioglu, L. A., Akilli, H. and Sarigiguzel, F., 2021. Analysis of Attack Angle Effect on Flow Characteristics Around Torpedo-Like Geometry Placed Near the Free-Surface via CFD. *Journal of Polytechnic-Politeknik Dergisi*, 24, 1579-1592. <https://doi.org/10.2339/politeknik.675632>
- [9] Degiuli, N., Farkas, A., Martic, I., Zeman, I., Ruggiero, V. and Vasiljevic, V., 2021. NUMERICAL AND EXPERIMENTAL ASSESSMENT OF THE TOTAL RESISTANCE OF A YACHT. *Brodogradnja*, 72, 61-80. <https://doi.org/10.21278/brod72305>
- [10] Ignacio, L. C., Victor, R. R., Francisco, D. R. R. and Pascoal, A., 2019. Optimized design of an autonomous underwater vehicle, for exploration in the Caribbean Sea. *Ocean Engineering*, 187. <https://doi.org/10.1016/j.oceaneng.2019.106184>
- [11] Luo, W., Guo, X., Dai, J. and Rao, T., 2021. Hull optimization of an underwater vehicle based on dynamic surrogate model. *Ocean Engineering*, 230. <https://doi.org/10.1016/j.oceaneng.2021.109050>
- [12] Li, C., Wang, P., Dong, H. and Wang, X., 2018. A simplified shape optimization strategy for blended-wing-body underwater gliders. *Structural and Multidisciplinary Optimization*, 58, 2189-2202. <https://doi.org/10.1007/s00158-018-2005-4>
- [13] Zhao, C., Wang, W., Jia, P. and Xie, Y., 2021. OPTIMISATION OF HULL FORM OF OCEAN-GOING TRAWLER. *Brodogradnja*, 72, 33-46. <https://doi.org/10.21278/brod72403>
- [14] Wang, X., Song, B., Wang, P. and Sun, C., 2018. Hydrofoil optimization of underwater glider using Free-Form Deformation and surrogate-based optimization. *International Journal of Naval Architecture and Ocean Engineering*, 10, 730-740. <https://doi.org/10.1016/j.ijnaoe.2017.12.005>
- [15] Vasudev, K. L., Sharma, R. and Bhattacharyya, S. K., 2018. Shape optimisation of an AUV with ducted propeller using GA integrated with CFD. *Ships and Offshore Structures*, 13, 194-207. <https://doi.org/10.1080/17445302.2017.1351292>
- [16] Liu, X., Yuan, Q., Zhao, M., Cui, W. and Ge, T., 2017. Multiple objective multidisciplinary design optimization of heavier-than-water underwater vehicle using CFD and approximation model. *Journal of Marine Science and Technology*, 22, 135-148. <https://doi.org/10.1007/s00773-016-0399-5>
- [17] Wu, S., Cai, M., Yang, C., Wu, W. and Wang, T., 2020. Hydrodynamic Shape Optimization of an Autonomous Underwater Vehicle With an Integrated Lifting Line and Viscous Continuous Adjoint Approach. *IEEE Journal of Oceanic Engineering*, 45, 851-861. <https://doi.org/10.1109/JOE.2019.2910939>
- [18] Dong, H., Wu, Z., Tan, M. and Yu, J., 2020. Hydrodynamic Analysis and Verification of an Innovative Whale Shark-like Underwater Glider. *Journal of Bionic Engineering*, 17, 123-133. <https://doi.org/10.1007/s42235-020-0010-y>
- [19] Sun, T., Chen, G., Yang, S., Wang, Y., Wang, Y., Tan, H. and Zhang, L., 2021. Design and optimization of a bio-inspired hull shape for AUV by surrogate model technology. *Engineering Applications of Computational Fluid Mechanics*, 15, 1057-1074. <https://doi.org/10.1080/19942060.2021.1940287>
- [20] Liu, J., He, B., Yan, T., Yu, F. and Shen, Y., 2021. Study on carbon fiber composite hull for AUV based on response surface model and experiments. *Ocean Engineering*, 239. <https://doi.org/10.1016/j.oceaneng.2021.109850>
- [21] Li, T. Z. and Yang, X. L., 2019. An efficient uniform design for Kriging-based response surface method and its application. *Computers and Geotechnics*, 109, 12-22. <https://doi.org/10.1016/j.compgeo.2019.01.009>

- [22] Solak, H. P., 2020. MULTI-DIMENSIONAL SURROGATE BASED AFT FORM OPTIMIZATION OF SHIPS USING HIGH FIDELITY SOLVERS. *Brodogradnja*, 71, 85-100. <https://doi.org/10.21278/brod71106>
- [23] Zhang, Y., Ho, S. L. and Fu, W., 2018. Applying Response Surface Method to Oil-Immersed Transformer Cooling System for Design Optimization. *IEEE Transactions on Magnetics*, 54. <https://doi.org/10.1109/TMAG.2018.2840337>
- [24] Guan, G., Yang, Q., Wang, Y., Zhou, S. and Zhuang, Z., 2021. Parametric design and optimization of SWATH for reduced resistance based on evolutionary algorithm. *Journal of Marine Science and Technology*, 26, 54-70. <https://doi.org/10.1007/s00773-020-00721-w>
- [25] Guan, G., Wang, L., Geng, J., Zhuang, Z. and Yang, Q., 2021. Parametric automatic optimal design of USV hull form with respect to wave resistance and seakeeping. *Ocean Engineering*, 235. <https://doi.org/10.1016/j.oceaneng.2021.109462>
- [26] An, X., Chen, Y. and Huang, H., 2021. Parametric Design and Optimization of the Profile of Autonomous Underwater Helicopter Based on NURBS. *Journal of Marine Science and Engineering*, 9. <https://doi.org/10.3390/jmse9060668>
- [27] Doss, A. S. A., Venkatesh, D. and Ovinis, M., 2021. SIMULATION AND EXPERIMENTAL STUDIES OF A MOBILE ROBOT FOR UNDERWATER APPLICATIONS. *International Journal of Robotics and Automation*, 36, 10-17. <https://doi.org/10.2316/J.2021.206-0424>
- [28] Gallimore, E., Stokey, R., Terrill, E. and Ieee, 2018. Robot Operating System (ROS) on the REMUS AUV using RECON. *IEEE/OES Autonomous Underwater Vehicle Workshop (AUV)*, Rectory Univ Porto, Porto, PORTUGAL. <https://doi.org/10.1109/AUV.2018.8729755>
- [29] Guo, H., Guo, C., Hu, J., Lin, J. and Zhong, X., 2021. Influence of jet flow on the hydrodynamic and noise performance of propeller. *Physics of Fluids*, 33. <https://doi.org/10.1063/5.0051326>
- [30] Tian, W., Song, B. and Ding, H., 2019. Numerical research on the influence of surface waves on the hydrodynamic performance of an AUV. *Ocean Engineering*, 183, 40-56. <https://doi.org/10.1016/j.oceaneng.2019.04.007>
- [31] Song, S., Demirel, Y. K. and Atlar, M., 2019. An investigation into the effect of biofouling on the ship hydrodynamic characteristics using CFD. *Ocean Engineering*, 175, 122-137. <https://doi.org/10.1016/j.oceaneng.2019.01.056>
- [32] Pu, L., Qi, D., Xu, L. and Li, Y., 2017. Optimization on the performance of ground heat exchangers for GSHP using Kriging model based on MOGAs. *Applied Thermal Engineering*, 118, 480-489. <https://doi.org/10.1016/j.applthermaleng.2017.02.114>
- [33] Mao, Z., Pi, Y., Li, B., Lu, C. and Tian, W., 2022. Parametric optimization for liquid cooling microchannels of AUV's battery thermal management system. *Journal of Thermal Analysis and Calorimetry*. <https://doi.org/10.1007/s10973-022-11241-7>
- [34] Sun, J., Zhang, W. and Dong, X., 2020. Natural Frequency Prediction Method for 6R Machining Industrial Robot. *Applied Sciences-Basel*, 10. <https://doi.org/10.3390/app10228138>
- [35] Mifsud, D. and Verdin, P. G., 2021. Surrogate-Based Design Optimisation Tool for Dual-Phase Fluid Driving Jet Pump Apparatus. *Archives of Computational Methods in Engineering*, 28, 53-89. <https://doi.org/10.1007/s11831-019-09373-5>

Submitted: 07.06.2022. Shuping Hou* (the corresponding author), houshuping@hrbeu.edu.cn
Zejiang Zhang, zhangzejiang@hrbeu.edu.cn

Accepted: 04.09.2022. Hongtai Lian, 396831102@qq.com
Xiaodong Xing, xingxiaodong@hrbeu.edu.cn
Haixia Gong, gonghaixia@hrbeu.edu.cn
College of Mechanical and Electrical Engineering, Harbin Engineering University, Harbin 150001, China
Xiujun Xu, xuxiujun@hrbeu.edu.cn
College of Intelligent Systems Science and Engineering, Harbin Engineering University, Harbin 150001, China